Research Square

Preprints are preliminary reports that have not undergone peer review.
They should not be considered conclusive, used to inform clinical practice,
or referenced by the media as validated information.

Growing-season Arctic carbon fluxes are changing relatively faster in tundra than in boreal ecosystems

Neus Sabater

neus.sabater@fmi.fi

Finnish Meteorological Institute https://orcid.org/0000-0002-0296-4378

Ella Kivimäki

Finnish Meteorological Institute https://orcid.org/0000-0002-8150-8775

Anna-Maria Virkkala

Finnish Meteorological Institute

Tea Thum

Finnish Meteorological Institute https://orcid.org/0000-0001-9216-1271

Juha Aalto

Finnish Meteorological Institute https://orcid.org/0000-0001-6819-4911

Miska Luoto

University of Helsinki https://orcid.org/0000-0001-6203-5143

Shari Van Wittenberghe

University of Valencia

Antti Lipponen

Finnish Meteorological Insitute https://orcid.org/0000-0002-6902-9974

Pekka Kolmonen

Finnish Meteorological Institute

Antti Arola

Finnish Meteorological Institute https://orcid.org/0000-0002-9220-0194

Article

Keywords: Solar-Induced Chlorophyll Fluorescence, Gross Primary Productivity, Ecosystem Respiration, Tundra, permafrost, Arctic

Posted Date: September 22nd, 2026

DOI: https://doi.org/10.21203/rs.3.rs-10905621/v1

License: This work is licensed under a Creative Commons Attribution 4.0 International License.
Read Full License

Additional Declarations: There is **NO** Competing Interest.

Growing-season Arctic carbon fluxes are changing relatively faster in tundra than in boreal ecosystems

Neus Sabater[1*], Ella Kivimäki[1], Anna-Maria Virkkala[2], Tea Thum[2], Juha Aalto[3,4], Miska Luoto[4], Shari Van Wittenberghe[5], Antti Lipponen[1], Pekka Kolmonen[1], Antti Arola[1]

[1*]Atmospheric Research Centre of Eastern Finland, Finnish Meteorological Institute, Erik Palménin aukio 1, Helsinki, 00560, Finland.
[2]Climate System Research Unit, Finnish Meteorological Institute, Erik Palménin aukio 1, Helsinki, 00560, Finland.
[3]Weather and Climate Change Impact Research, Finnish Meteorological Institute, Erik Palménin aukio 1, Helsinki, 00560, Finland.
[4]Department of Geosciences and Geography, University of Helsinki, Gustaf Hällströmin katu 2a, Helsinki, 00014, Finland.
[5]Laboratory for Earth Observation, Image Processing Laboratory, University of Valencia, Catedrático Agustín Escardino 9, Paterna, 46980, Spain.

*Corresponding author(s). E-mail(s): neus.sabater@fmi.fi;
Contributing authors: ella.kivimaki@fmi.fi; anna-maria.virkkala@fmi.fi; tea.thum@fmi.fi; juha.aalto@fmi.fi; miska.luoto@helsinki.fi; shari.wittenberghe@uv.es; antti.lipponen@fmi.fi; pekka.kolmonen@fmi.fi; antti.arola@fmi.fi;

Abstract

Rapid Arctic warming is altering ecosystem functioning and challenging the view of the terrestrial Arctic as a sustained carbon sink. Drawing on independent evidence from warming experiments, satellite observations, data-driven eddy-covariance-based flux products, and atmospheric inversions, we assess growing-season carbon dioxide (CO_2) fluxes across the terrestrial Arctic (60°N–90°N) between 2001 and 2020. We find that tundra ecosystems exhibit larger relative increases in gross primary productivity (median 7–8%) than boreal regions (median 4–5%), which is also reflected in larger relative increases in solar-induced chlorophyll fluorescence (median 9% versus 5%) and an overall strengthening of carbon uptake (median of 9–11% versus 3–5%) between the two decades. Despite differences among datasets, their agreement on broad-scale patterns suggests that Arctic warming is reshaping tundra carbon dynamics faster than those of boreal ecosystems.

Keywords: Solar-Induced Chlorophyll Fluorescence, Gross Primary Productivity, Ecosystem Respiration, Tundra, permafrost, Arctic

Over the past four decades, the Arctic has warmed nearly four times faster than the global average, a phenomenon known as Arctic amplification [1–3]. This rapid warming, together with rising atmospheric carbon dioxide (CO_2), has increased vegetation productivity across the extratropical Northern Hemisphere since the 1980s [4, 5]. However, the persistence of these trends under continued climate change remains uncertain [5, 6]. Satellite and in situ observations reveal widespread Arctic greening, driven by longer growing seasons, enhanced photosynthesis, and shifts in plant community composition [7–12]. Yet, this trend is punctuated by regional browning events linked to disturbances (e.g., winter warming, wildfires) and processes such as permafrost thaw and hydrological change [13–17].

These vegetation dynamics directly affect the Arctic carbon cycle [10, 18]. Most terrestrial carbon exchange occurs during the growing season, when both gross primary productivity (GPP) and ecosystem respiration (ER) increase. However, because NEE represents the relatively small difference between these two large fluxes, it remains difficult to constrain and varies strongly across space and time [19–23]. For a broader overview of Arctic terrestrial carbon cycling, see Natali et al.[24].

In the terrestrial Arctic (60°N–90°N), while early growing-season increases in photosynthesis may enhance carbon uptake, they can be offset by increased late-season respiration, limiting annual net sequestration [25, 26]. As a result, some regions may already function as annual net CO_2 sources [27], even though the broader Arctic–Boreal region has remained a net sink over recent decades [28]. The magnitude and direction of these responses are likely to differ between tundra and boreal ecosystems owing to contrasts in vegetation structure, productivity, disturbance regimes, hydrology, and permafrost influence. These uncertainties are further amplified by the sparse and uneven distribution of in situ observations, complicating efforts to quantify the carbon balance in the terrestrial Arctic zone [29].

To address these limitations, machine-learning approaches have been developed to upscale CO_2 flux observations from eddy covariance (EC) and chamber measurements using satellite and meteorological data [30–36]. In parallel, satellite-derived solar-induced chlorophyll fluorescence (SIF) has emerged as a robust proxy for photosynthetic activity and is increasingly used to evaluate large-scale GPP estimates [37–41].

Here, we examine how tundra and boreal ecosystems differ in their responses to recent warming, with particular emphasis on relative changes in growing-season carbon fluxes. We test whether independent datasets spanning up to two decades in most cases converge on a consistent picture of the Arctic growing-season carbon balance. In particular, we use independent model-driven datasets based on (i) experimental warming responses of ecosystem respiration [19], (ii) eddy covariance–based estimates of GPP and NEE combined with satellite predictors [36, 42], and (iii) satellite observations of SIF [43]. Also, to complement the bottom-up data-driven C flux balance assessment, we use an ensemble of different top-down atmospheric inversion models [44].

Results

Heterogeneous increases in Arctic gross primary productivity

Across the terrestrial Arctic, growing-season (June–August, JJA) gross primary production (GPP) increased robustly between the two decades of our study period (2001–2010 vs. 2011–2020), with remarkably consistent median increases of approximately 5–6% across two independent, data-driven products, X-BASE [36] and FluxSat [42] (Table 1). This tendency aligns with previous observations [45, 46] and is supported by an increase in solar-induced fluorescence (SIF; median of 6.5%), reinforcing evidence for a widespread intensification of photosynthetic activity during the growing season.

The spatial pattern of change (Fig. 1.a–c) is heterogeneous across the terrestrial Arctic but remains broadly consistent across datasets. After restricting the analysis to pixels with relative changes between -100 and 100%, relative changes in SIF were positively correlated with relative changes in GPP from both X-BASE ($r = 0.38$, $n = 1.21 \times 10^6$) and FluxSat ($r = 0.79$, $n = 1.12 \times 10^6$), supporting the consistency of the large-scale spatial patterns across independent products. The strongest increases, in relative terms, occur in tundra-dominated regions, including eastern Canada (CAN.E) and the Taymyr Peninsula (RUS), where GPP increases exceed 10% and are accompanied by even larger SIF enhancements (10%–17%, see Table 1). In contrast, other localized regions exhibit weak or negligible changes lower than 2%, such as parts of the southern Canadian Archipelago (CAN.A.S) and northern Fennoscandia (FEN), while Alaska (AK) shows a mixed response. Notably, areas with limited or negative GPP transitions consistently coincide with weak SIF changes, suggesting the expected physically consistent link between SIF and GPP across datasets.

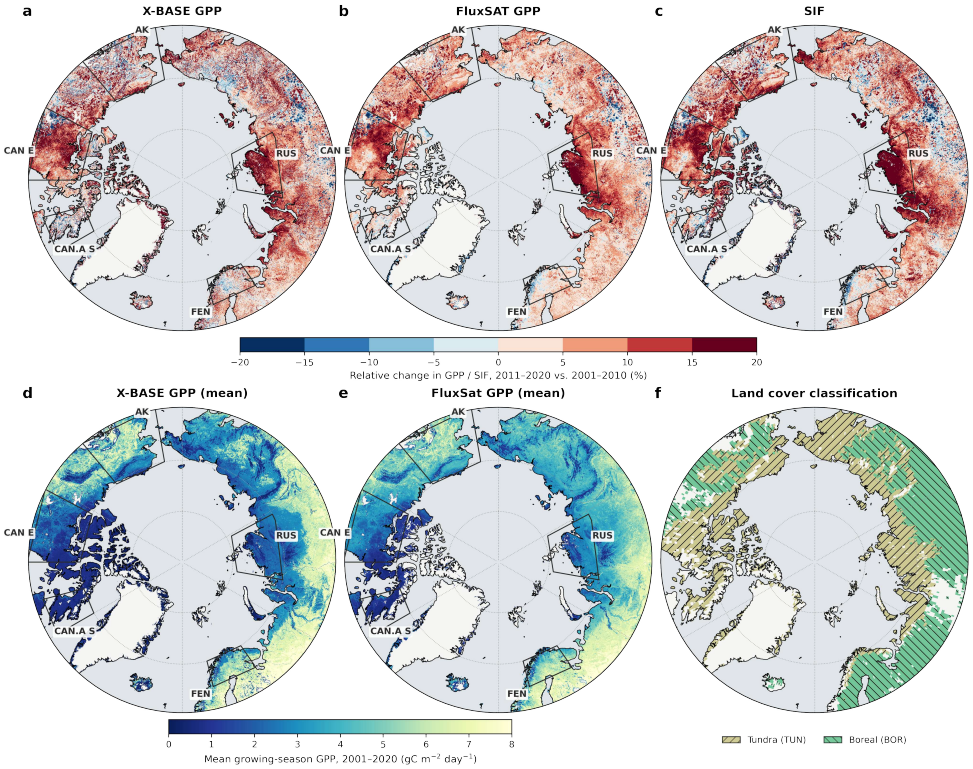


Fig. 1: **Spatial Patterns in gross primary productivity (GPP) and Solar-induced Fluorescence (SIF) decadal changes**. GPP transition between the second (2011-2020) and first (2001-2010) periods evaluated for the X-BASE and FluxSat datasets (**a** and **b**, respectively). SIF transition between the same periods (**c**). Mean climatological GPP values for the entire period of 2001-2020 for the X-BASE and FluxSat datasets (**d** and **e**, respectively). Tundra and Boreal areas according to the BALWD classification [47]**(f)**. Geographical abbreviations refer to Alaska (AK), eastern Canada (CAN.E), the southern Canadian Archipelago (CAN.A.S), northern Fennoscandia (FEN), and the Taymyr Peninsula, Russia (RUS).

Comparison of relative changes of GPP between decades against long-term mean productivity (referred here as "GPP climatology") across the 2001–2020 period reveals a clear biome-dependent pattern (Fig. 1). Low-productivity tundra systems exhibit the largest relative increases (5–6%), whereas more productive boreal regions show smaller relative gains (2-3%) (see Table 1). In this manuscript, we refer to tundra and boreal regions (Fig. 1.f) as defined by the BAWLD classification [47], where tundra

and boreal classes correspond to pixels with the highest percentage cover of dry tundra and boreal forest, respectively (See Supplementary Fig. A2 for percent maps). We also observe a higher sensitivity of SIF response to warming (air temperature increase, see Methods for this analysis) in those pixels with a higher percentage of dry tundra presence compared to boreal forest (Supplementary Fig. A3), while this behaviour is more inconclusive for GPP (Supplementary Fig. A3, A9, A10 and Tables A4 and A5). Many factors potentially drive the response of GPP, such as the subclimatic zone [48], the vegetation type and abundance, nutrient availability [49], the C stock (including the above-ground biomass) [50, 51] or the permafrost presence [52, 53], which modulate the resilience of the biome to increasingly more frequent drastic changes [17] and Arctic warming. Consistent with this interpretation, we further observe enhanced sensitivity of GPP to air temperature—expressed through its linear response (Supplementary Table A6)—in regions characterized by higher permafrost presence, as identified from thermokarst classifications [52]. Although indirectly, this points to the role of permafrost-affected landscapes as key modulators of productivity and greening responses under warming [54, 55].

When comparing the decadal changes in GPP reported by each dataset, i.e., FluxSat and X-BASE, an interesting spatial pattern emerges differentiating between over- and under-estimated areas (Fig. 2.a). These highlighted areas perfectly align with the biome boundaries defined by the IGBP classification used in the X-BASE construction [56]. According to the IGBP classification, X-BASE estimates higher GPP changes in boreal forests (e.g., IGBP classes of Deciduous and Evergreen Needle-leaf Forest in Fig. 2.c), whereas FluxSat reports higher values of decadal change in tundra ecosystems (e.g., Open Shrubs and Grasslands) and Wetlands. Such an observed dependency on the IGBP classification most likely reflects sensitivities to model structure and training data in the generation of the X-BASE dataset. Because GPP is a dominant component of the growing-season carbon balance, these discrepancies do

not obscure the broad large-scale patterns observed across datasets, but instead highlight remaining uncertainties in the magnitude and spatial distribution of productivity responses to warming. This calls for targeted experiments and benchmarking to disentangle how differences in machine-learning architectures, predictor variables, and training datasets shape spatial patterns of Arctic carbon fluxes.

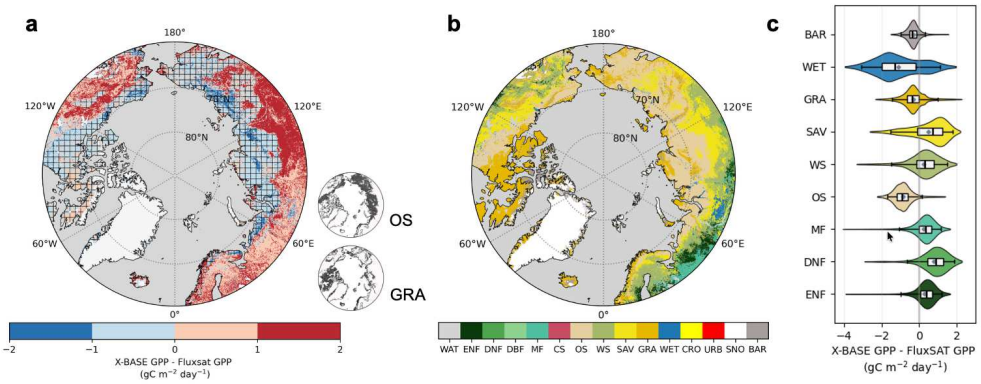


Fig. 2: **Divergent Decadal GPP Transitions Across the terrestrial Arctic Land-Cover Types** . Discretized map of the decadal GPP transition differences between X-BASE and FluxSat with an overlapping gridded square pattern on the IGBP classes of Open Shrublands (OS) and grasslands (GRA) (**a**). Classification of the IGBP land-cover class map [56], using data from year 2020 (**b**).Violin plots showing the statistics of the decadal GPP transition differences between the X-BASE and FluxSat databases during the growing season (JJA) (**c**). IGBP land-cover classes: Evergreen Needleleaf Forest (ENF), Evergreen Broadleaf Forest (EBF), Deciduous Needleleaf Forest (DNF), Deciduous Broadleaf Forest (DBF), Mixed Forest (MF), Closed Shrublands (CSH), Open Shrublands (OSH), Woody Savannas (WSA), Savannas (SAV), Grasslands (GRA), Permanent Wetlands (WET), Croplands (CRO), Urban and Built-up (URB), Cropland–Natural Vegetation Mosaic (MOS), Snow and Ice (SNO), Barren or Sparsely Vegetated (BAR), and Water Bodies (WAT).

Table 1: **Summary of growing-season (JJA) carbon flux changes across datasets.** Values are reported as the median and the interquartile range (IQR). The ΔGPP(NEE) refers to changes between the two decades, i.e., 2011–2020 minus 2001–2010. GPP units are gC m^{-2} day^{-1} or in percent. Negative NEE values indicate a shift towards enhanced C uptake. For the ER, the reported values correspond to the slope of the linear regression following $\Delta ER = \alpha \Delta T_{air} + n$ for the combined (ER_{COM}) and the X-BASE ($ER_{X\text{-}BASE}$) products. The ER experiment section reports the percent median values of the regions and the (IQR) associated with the percent maps provided in [19]. The values marked with * correspond to the whole map provided by [19] which mostly covers tundra landscapes. For more details regarding the statistics, see Supplementary Tables A2 and A3. The acronyms of the regions refer to CAN.E (Canada East), RUS (Taymyr region in Russia), CAN.A S (Canadian Archipelago South), FEN (Northern Fennoscandia) and AK (Alaska); the ER-experiment section instead uses Y-G (Yamal–Gydan), CAN.A (Canadian Archipelago) and RUS.E (East Russia) – a different, coarser set of polygons specific to that dataset (see note below). The limits used to define all regions are given in Supplementary Table A2.

Gross Primary Production (GPP)			
Metric / Region	$\Delta GPP_{X\text{-}BASE}$ (%) median (IQR)	$\Delta GPP_{FluxSat}$ (%) median (IQR)	ΔSIF (%) median (IQR)
Pan-Arctic change	5.56 (0.66 – 11.6)	5.61 (2.25 – 9.81)	6.5 (1.29 – 12.29)
CAN.E	9.99 (5.23 – 15.95)	9.57 (5.72 – 13.39)	10.41 (5.52 – 15.15)
RUS (Taymyr)	12.64 (8.19 – 18.59)	13.22 (9.85 – 17.42)	17.36 (11.09 – 24.93)
CAN.A S	0.34 (−5.42 – 4.64)	0.95 (−2.38 – 4.35)	1.31 (−4.56 – 7.05)
FEN	1.94 (−2.22 – 5.95)	1.45 (−1.22 – 3.89)	1.23 (−2.11 – 4.27)
AK	3.19 (−1.49 – 9.27)	5.90 (2.96 – 9.12)	5.61 (1.2 – 11.01)
Tundra change	7.34 (1.69 – 13.62)	7.46 (3.46 – 11.65)	9.1 (3.73 – 14.95)
Boreal change	3.98 (0.02 – 8.24)	4.35 (1.72 – 7.58)	4.13 (−0.05 – 8.54)
Metric / Region	$\Delta GPP_{X\text{-}BASE}$ (gC m^{-2} day^{-1}) median (IQR)	$\Delta GPP_{FluxSat}$ (gC m^{-2} day^{-1}) median (IQR)	
Tundra (climatology)	2.12 (0.92 – 2.82)	3.00 (1.88 – 3.82)	—
Boreal (climatology)	5.94 (3.88 – 6.92)	5.28 (4.27 – 6.41)	—
Net Ecosystem Exchange (NEE)			
Metric / Region	$\Delta NEE_{X\text{-}BASE}$ (%) median (IQR)	ΔNEE_{COM} (%) median (IQR)	$\Delta C\ flux_{atm\text{-}inv}$ (%) median (IQR)
Pan-Arctic	−5.58 (−20.12 – 4.21)	−6.58 (−17.95 – 3.71)	—
CAN.A S	5.33 (−10.85 – 22.72)	1.58 (−18.93 – 15.49)	—
RUS (Taymyr)	−19.07 (−37.02 – −7.48)	−16.47 (−26.75 – −9.68)	—
Tundra	−10.1 (−27.71 – 2.25)	−8.91 (−19.1 – −0.3)	−11.48 (−30.75 – 6.13)
Boreal	−2.71 (−11.38 – 4.81)	−4.39 (−16.69 – 7.11)	−5.18 (−15.71 – 10.64)
Ecosystem Respiration (ER)			
Metric / Region	$\alpha(\Delta ER_{X\text{-}BASE})$ slope (CI)	$\alpha(\Delta ER_{COM})$ slope (CI)	Experiment (%) median (IQR)
Y-G	0.11 (0.09 – 0.13)	0.17 (0.15 – 0.20)	35.73 (24.24 – 49.93)
CAN.A	0.04 (0.02 – 0.05)	0.07 (0.05 – 0.10)	26.85 (21.93 – 33.46)
RUS.E	0.09 (0.06 – 0.12)	0.12 (0.08 – 0.17)	38.57 (28.77 – 49.62)
Tundra	0.06 (0.04 – 0.10)	0.11 (0.07 – 0.15)	27.52 (21.41 – 35.81)%*

Contrasting ecosystem respiration responses to warming

In tundra ecosystems, controlled warming experiments (+1.4°C in air and +0.4°C in soil) reported an overall increase in ecosystem respiration (ER) of approximately 30% [19]. We use the ER change map (Fig. 3a) derived from warming experiment data during the growing season [19] as a benchmark against warming-induced ER changes inferred from X-BASE and FluxSat. Given that the extension of the experimental-based map of ER covered only tundra regions, we use the Circumpolar Arctic Vegetation Map (CAVM) [57] to enrich the interpretation (Fig.3.b) and capture the heterogeneity of tundra-dominated landscapes.

According to the experimental-based map [19], the Yamal–Gydan region (Y-G) shows the strongest increase in ER (median of ≈37%), whereas the Canadian Archipelago (CAN.A) exhibits consistently weaker (median of ≈27%) responses to warming. Eastern Siberia (RUS.E) presents a more heterogeneous pattern, with both high and low responses depending on local vegetation composition (Table1). These contrasts align with differences in vegetation structure and biomass: Y-G is characterized by shrub- and sedge-dominated tundra with relatively high aboveground biomass, while CAN.A is dominated by sparsely vegetated barrens and low-productivity tundra types (see Fig.3.b). Eastern Siberia (RUS.E) reflects a mixture of these tundra types, resulting in intermediate and spatially variable ER warming-induced change.

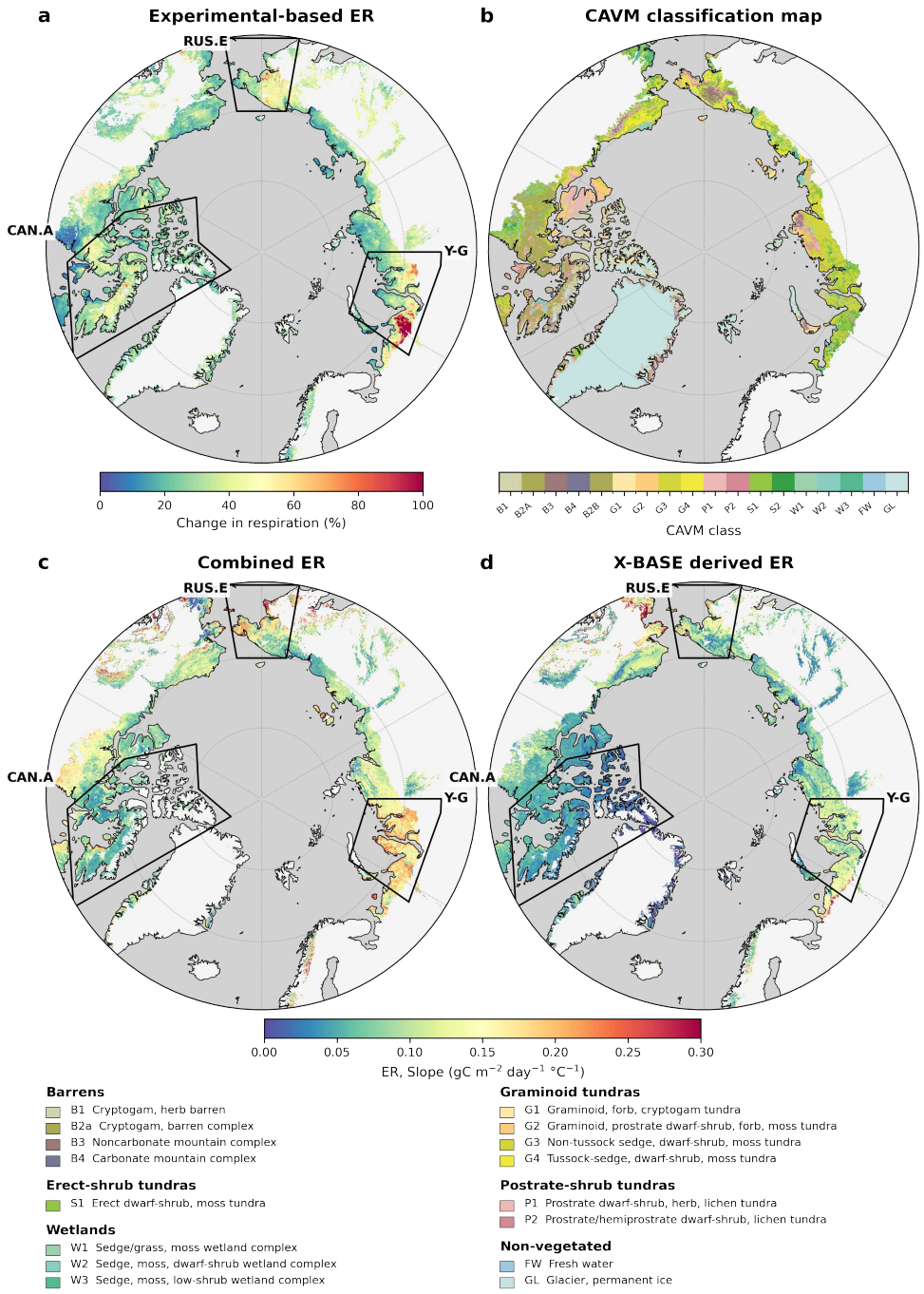


Fig. 3: **Ecosystem Respiration (ER) warming response.** Change in percent of ER due to an increase in temperature of 1.4 °C in air and 0.4°C in soil. Data origin [19](a). CAVM tundra classification map (b). ER change associated with an increase in air temperature of 1.4 °C and represented by the slope (α) of the linear regression in $\Delta ER = \alpha \Delta T_{air} + n$ for the combined ($\mathrm{ER_{COM}}$) and the X-BASE ($\mathrm{ER_{X\text{-}BASE}}$) products (c) and (d), respectively.

Because ER is not directly provided in FluxSat or X-BASE, we derive it from GPP and NEE using $NEE = ER - GPP$, assuming a closed C cycle. This results in two products: $\mathrm{ER_{X\text{-}BASE}}$ and $\mathrm{ER_{COM}}$, the latter from combining FluxSat GPP with X-BASE NEE. To enable an spatial comparison with the experimental-based map ($\mathrm{ER_{exp}}$), we adopt a simplified linear temperature response of ER to air temperature changes across 2001-2020 during the growing season, e.g., $\Delta ER = \alpha \Delta T_{air} + n$, expressing anomalies of ΔER and ΔT_{air} relative to the 2001–2020 climatology (see Methods). Although ER responses to temperature are often represented as non-linear functions—either monotonic (with or without saturation) or exhibiting an optimum [20]—this linear approximation is assumed to facilitate the spatial comparison across datasets.

The spatial distribution of the inferred response of ER to warming, that is indicated by the slope α (Fig. 3.c,d), is consistent with the spatial pattern derived from the experimental datasets $\mathrm{ER_{exp}}$ (Fig. 3.a). Regions with low-biomass content and dominated by barrens (e.g., CAN.A) show weaker temperature sensitivity, whereas shrub- and sedge-dominated tundra regions (e.g. Y-G) exhibit stronger responses. Across all tundra regions, despite the general agreement on the spatial gradients, $\mathrm{ER_{COM}}$ consistently shows higher sensitivities to warming than $\mathrm{ER_{X\text{-}BASE}}$.

A direct one-to-one comparison between $\mathrm{ER_{exp}}$ and the linear responses modelled in $\mathrm{ER_{X\text{-}BASE}}$ and $\mathrm{ER_{COM}}$ must be done cautiously due to the different assumptions underlying each dataset. Nevertheless, it is possible to estimate the absolute change in ER (g C $\mathrm{m^{-2}}$ $\mathrm{day^{-1}}$) for $\mathrm{ER_{X\text{-}BASE}}$ and $\mathrm{ER_{COM}}$ by assuming a 1.4 °C increase in air temperature and using the climatological ER mean for 2001–2020 (see Supplementary Material). The estimates from the warming-induced experiment report higher values (Supplementary Material, Fig. A4) most probably reflecting discrepancies associated with the data origin and differing auxiliary datasets used for spatially continuous

upscaling. For instance, while the campaign-based experiments incorporated soil carbon (C) and nitrogen (N) spatial information for the metaregression-modeled maps [19], these auxiliary variables were not explicitly used in the EC-derived linear regression products [36, 42]. However, despite the expected discrepancies among datasets derived from fundamentally different approaches and datasets, the emergence of coherent spatial patterns across all evaluated regions lends confidence to the identified hotspots of ecosystem response to warming.

Implications for growing-season net ecosystem exchange

The warming-induced response of the growing-season C balance reflects the interplay between enhanced GPP and ER. Decadal changes (ΔNEE), defined as differences between 2011–2020 and 2001–2010 in JJA, indicate shifts in the strength of net carbon exchange. Because NEE is defined as positive (C release) and negative (C uptake), ΔNEE does not indicate whether an ecosystem functions as a net carbon source or sink, but rather whether carbon exchange has shifted towards greater uptake or release between decades. Accordingly, a negative ΔNEE indicates stronger carbon uptake or weaker carbon release, whereas a positive ΔNEE indicates stronger carbon release or weaker carbon uptake.

Both NEE products ($NEE_{X\text{-}BASE}$ and NEE_{COM}, see Methods) show consistent spatial patterns (see Supplementary Figs. A5, A6, A7, and A8 for yearly basis), with an overall median decrease of ≈6–7 % between the two decades evaluated across the terrestrial Arctic during the growing season, indicating a tendency towards reduced C release (Fig. 4 and Table 1).

Regionally, however, the magnitude of this shift towards reduced C release (or increase) varies substantially. Both products report in the southern Canadian Archipelago (CAN.A S) a weak positive ΔNEE, accompanied by high variability,

suggesting that low-productivity systems may not fully offset warming-enhanced respiration. In contrast, the Taymyr Peninsula (RUS) exhibits a marked decrease in ΔNEE (enhanced carbon uptake), consistent with stronger increases in GPP.

However, when comparing relative changes in NEE with those in net land carbon flux derived from atmospheric inversion models over the same period [44], some discrepancies appear in the regional patterns. A direct one-to-one evaluation between the atmospheric inversion models and bottom-up land flux estimates would require accounting for lateral carbon transport (e.g., aquatic fluxes), which is not considered here. Instead, we focus on assessing the consistency of spatial variability and decadal shifts across approaches and the overall statistics. In Fig.4, relative decadal changes of the net C land flux are shown together with the data-driven ΔNEE corresponding shifts. Despite the observed spatial variability, a consistent large-scale signal emerges across both data-driven and atmospheric inversion products: tundra ecosystems exhibit larger relative changes than boreal regions. Atmospheric inversion models indicate changes of approximately -11% in tundra compared with -5% in boreal areas, whereas EC-based products indicate changes ranging from -9 to -10% and from -3 to -4%, respectively (Fig. 5; Table A2). This pattern is further reinforced by the distribution of decadal transitions, for which the integrated area associated with negative flux changes is consistently larger in tundra than in boreal ecosystems across both atmospheric inversion models and EC-based products. The fraction of the distribution associated with negative transitions reaches 68.6%, 70.8%, and 75.6% for the atmospheric inversion ensemble, $\mathrm{NEE_{X\text{-}BASE}}$, and $\mathrm{NEE_{COM}}$, respectively, in tundra ecosystems, compared with 60.8%, 59.8%, and 61.5% in boreal regions (Fig. 5; Table A2). Notably, the integrated negative area exceeds 50% in all cases, indicating a prevailing tendency towards enhanced carbon uptake during the decadal transition, with this tendency being consistently more pronounced in tundra than in boreal ecosystems.

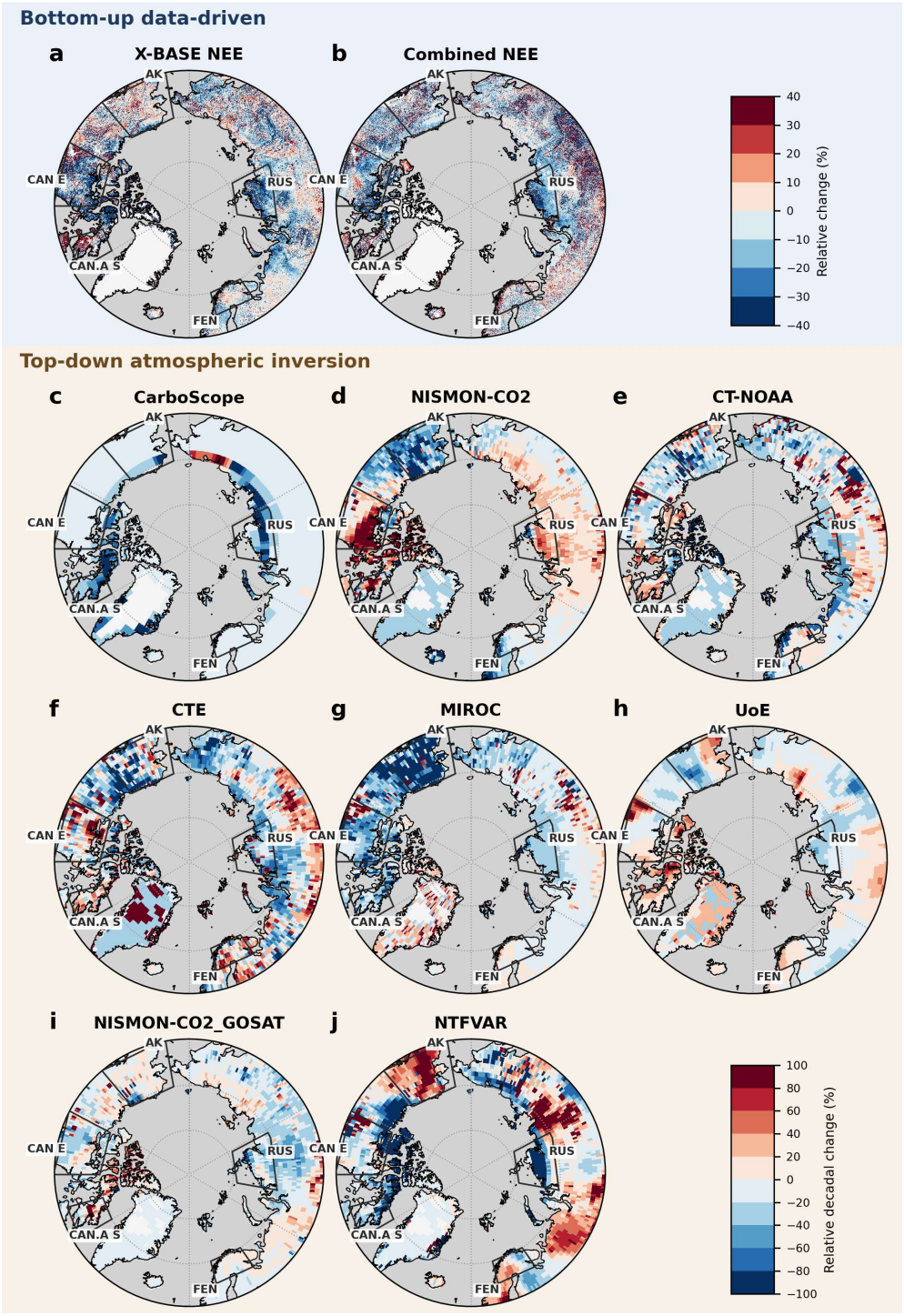


Fig. 4: **NEE decadal relative changes.** Decadal relative changes—defined as differences between 2011–2020 and 2001–2010— with respect to the mean absolute NEE value, e.g., ΔNEE/$|\ \overline{NEE}\ |$ in percent. Using absolute mean values makes the sign of the relative change reflect the direction of the shift, rather than its source–sink state. Data-driven X-BASE $NEE_{\text{X-BASE}}$ dataset (a) and the Combined NEE_{COM} dataset (b). Also, decadal relative transitions of the net land C flux reported by different atmospheric inversion models of CarboScope, NISMON-CO2, MIROC, UoE, NISMON-CO2_GOSAT, NTFVAR, CT-NOAA, CTE (c-j) [44]. The mean absolute value of NEE (or net C flux) is used, so the sign of the relative change indicates a relative increasing or decreasing tendency.

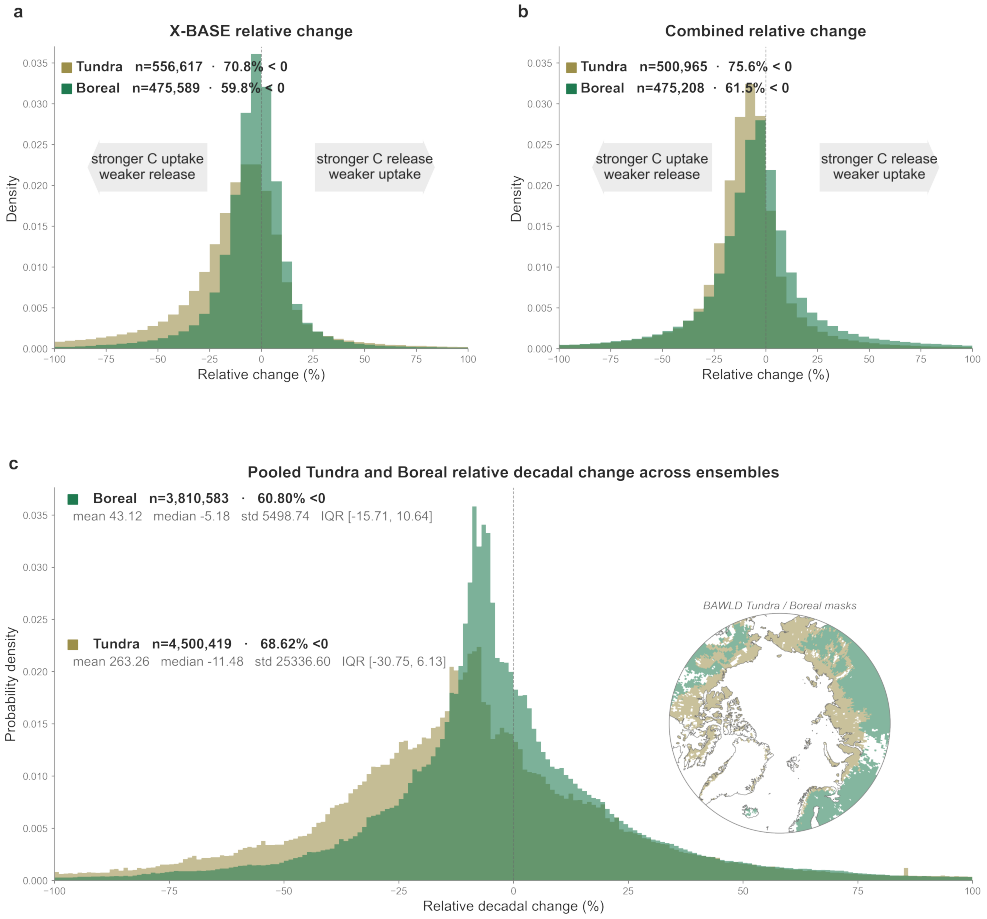


Fig. 5: **Distribution of the NEE and net C flux relative change across two decades.** Probability Density Function (PDF) of the $NEE_{X\text{-}BASE}$ (a) and NEE_{COM} (b) decadal transitions. Probability Density Function (PDF) of the net C flux from an ensemble of different atmospheric inversion C models (CarboScope, NISMON-CO2, CT-NOAA, MIROC, UoE, NISMON-CO2-GOSAT, NTFVAR [44]). Decadal transitions are reported in percent and are defined as differences between 2011–2020 and 2001–2010 with respect to the mean absolute NEE (or C flux) value. The mean absolute value is used so the positive (negative) values in the transition indicate regions pointing either toward a stronger (weaker) C release or a weaker (stronger) C uptake (a). PDFs are evaluated according to the BALWD dominant class of tundra or boreal forest.

Growing-season C source–sink behaviour across Arctic vegetation classes

We assess the distribution of growing-season NEE daily values across the two decades at the ecosystem level. According to the CAVM classification (Fig.3.b), most barren complexes (B1, B2a, B3, B4), prostrate shrub tundra (P1, P2), wet tundra complexes (W1, W2), and some graminoid tundra classes (G1, G3) exhibit a larger fraction of positive NEE values in the $NEE_{X\text{-}BASE}$ product, indicating a tendency towards net carbon release during the growing season (Fig. 6; Supplementary Fig. A12). The probability density functions (PDFs) of growing-season NEE values over 2001–2020 reveal that this source-like tendency is consistently more pronounced in $NEE_{X\text{-}BASE}$ than in NEE_{COM}. Differences in distribution shape (predominantly unimodal in $NEE_{X\text{-}BASE}$ versus bimodal in NEE_{COM}) likely reflect contrasting sensitivities to methodological constraints associated with the IGBP land-cover classification and the low number of flux sites in some of these classes [29].

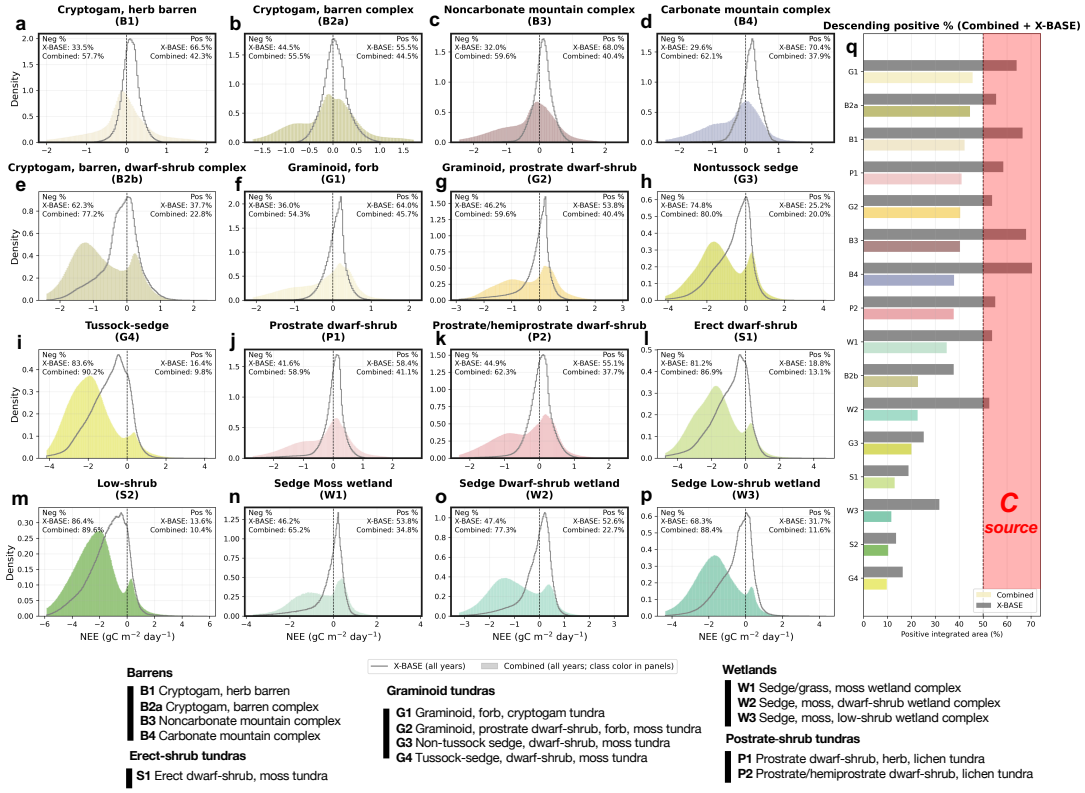


Fig. 6: **Probability Density function (PDF) of $NEE_{X\text{-}BASE}$ and NEE_{COM} values for the 2001-2020 period across the CAVM classification.** Histograms of $NEE_{X\text{-}BASE}$ (shaded color) and NEE_{COM} (gray line edge) PDF normalized for the 2001-2020 period across the CAVM classification (a-p). Panels of classes with the highlighted frame (B1, B2a, B3, B4, G1, G2, P1, P2, W1, and W2) are those with higher than 50% percent of $NEE_{X\text{-}BASE}$ positive values. Horizontal bar graph sorted in descending order of the percentage of NEE_{COM} positive values per CAVM class (q). NEE_{COM} in the color bar and $NEE_{X\text{-}BASE}$ in gray. For this per-class comparison, only those pixels for which data were available in both products were selected (see Methods).

The relative contribution of positive NEE values further highlights these differences. For several ecosystem classes, the $NEE_{X\text{-}BASE}$ estimates exceed the 50% threshold, indicating that positive NEE values dominate the distribution (Fig. 6.q). By contrast, NEE_{COM} generally shows a greater contribution from negative NEE

values, consistent with a prevailing growing-season carbon sink across both decades (Supplementary Fig. A11).

Discussion

Our results show that growing-season carbon cycling changed more strongly in tundra than in boreal ecosystems between 2001–2010 and 2011–2020. Both satellite- and EC-based data-driven products indicate larger relative increases in GPP and SIF in tundra regions than in boreal areas (Fig. 1, Table 1, and Supplementary Fig. A1). These results suggest that the largest responses to recent warming are occurring in low-productivity Arctic landscapes. However, the undergoing more rapid transformation in tundra than boreal systems, may respond not only to the lower productivity in absolute terms but to a set of different mechanisms likely involving interacting controls related to vegetation composition, hydrology, nutrient availability, disturbance regimes, and permafrost dynamics [8, 13, 58–60]. The strongest increases in productivity were concentrated in tundra-dominated regions of eastern Canada and the Taymyr Peninsula, whereas weaker or locally negative changes occurred in parts of Alaska, Fennoscandia, and the Canadian Archipelago. Such contrasts reinforce the notion that Arctic greening is not a spatially uniform process [8]. Instead, ecosystem responses emerge from the interaction of regional climate forcing with local environmental constraints [16, 60]. We also observed that an enhancement of GPP sensitivity overlaps regions with extensive permafrost and large carbon reservoirs (Supplementary Table A6)[50, 61], which further indicates the role played by warming-induced changes in soil thermal regimes, hydrology, and nutrient cycling in shaping future ecosystem productivity [62, 63]. Permafrost thaw can initially enhance vegetation productivity through increased nutrient availability and active-layer deepening, but these potential benefits may be offset by waterlogging, surface subsidence, and vegetation disturbance. The

balance between these effects likely depends on the extent and hydrological consequences of thaw and may shift over longer timescales [54]. Understanding how such transient belowground changes translate into shifts in vegetation abundance, plant species composition, productivity, and photosynthetic activity remains a key challenge for predicting Arctic carbon–climate feedbacks.

Our results demonstrate that, despite substantial spatial variability, experimental and data-driven approaches converge on similar large-scale patterns of ER sensitivity [64] (Fig. 3, Supplementary Fig. A4). This consistency suggests that the primary controls governing the spatial distribution of ER responses to warming are well captured across fundamentally different approaches. However, the systematically weaker temperature sensitivities inferred from data-driven products relative to experimental warming estimates indicate that deriving ER from NEE and GPP products using a simplified linear dependence on air temperature may not fully capture respiration responses to warming [65]. Nevertheless, the recurrent identification of regions such as the Yamal–Gydan Peninsula as hotspots of ER sensitivity increases confidence in the location of the strongest respiration responses, even if their absolute magnitude remains uncertain.

Decadal changes in growing-season net carbon balance revealed a consistent large-scale pattern across both EC-based data-driven and atmospheric inversion models: tundra ecosystems exhibited a more pronounced strengthening of carbon uptake than boreal regions (Fig. 5). Despite differences among products, this consistent pattern indicates that tundra landscapes are undergoing the largest relative changes in carbon cycling across the terrestrial Arctic. Our findings therefore suggest an Arctic carbon balance that is strengthening on average during the growing season, but in a highly heterogeneous way. Low-productivity systems such as the Canadian Archipelago show weak positive NEE transitions between decades, suggesting that respiration increases can outpace productivity gains, whereas more productive tundra regions such as the

Taymyr Peninsula exhibit strong shifts toward carbon uptake, supported by both higher baseline productivity and stronger GPP increases [8, 16]. The temporal analysis further indicates that warmer growing seasons do not systematically translate into enhanced carbon uptake (Supplementary Fig. A11), reflecting the tight coupling between GPP and ER and the influence of interannual variability, ecosystem-specific sensitivities, and legacy effects from previous seasons [66–71].

Importantly, stronger carbon uptake in tundra does not imply that all Arctic vegetation types are becoming stronger carbon sinks. Several High Arctic ecosystem classes, including barren, graminoid, prostrate-shrub, and wet tundra systems, frequently exhibit source-like behaviour during the growing season. However, the extent of this behaviour remains sensitive to the observational framework employed. Given the sparse and uneven distribution of in situ observations across large regions of the Arctic, estimating ecosystem-scale carbon fluxes inevitably requires the use of auxiliary information to generate spatially continuous products. Differences in how these auxiliary constraints are represented, including land-cover classifications and environmental predictors, contribute to uncertainty in source–sink attribution at the ecosystem level. These results therefore highlight both the complexity of Arctic carbon dynamics and the continued need for improved observational constraints in sparsely monitored regions [29]. Advancing observational capabilities will therefore be critical, particularly in regions where strong productivity responses overlap extensive permafrost and large carbon reservoirs. In particular, current and emerging satellite observations of vegetation fluorescence, together with visible, thermal infrared, and microwave measurements, offer new opportunities to characterize ecosystem productivity, respiration controls, hydrological change, and ecosystem responses to permafrost thaw [53, 72–75]. These advances will be crucial for understanding why tundra is changing faster than boreal ecosystems and for predicting the future trajectory of the terrestrial Arctic carbon cycle.

References

[1] Rantanen, M. *et al.* The Arctic has warmed nearly four times faster than the globe since 1979. *Communications Earth & Environment* **3**, 1–10 (2022).

[2] Zhou, W., Leung, L. R. & Lu, J. Steady threefold Arctic amplification of externally forced warming masked by natural variability. *Nature Geoscience* **17**, 508–515 (2024).

[3] Screen, J. A. *et al.* Causes and consequences of Arctic amplification elucidated by coordinated multimodel experiments. *Communications Earth & Environment* (2025).

[4] Zhu, Z. *et al.* Greening of the Earth and its drivers. *Nature climate change* **6**, 791–795 (2016).

[5] Zhang, Y. *et al.* Future reversal of warming-enhanced vegetation productivity in the Northern Hemisphere. *Nature Climate Change* 1–6 (2022).

[6] Xu, L. *et al.* Temperature and vegetation seasonality diminishment over northern lands. *Nature climate change* **3**, 581–586 (2013).

[7] Berner, L. T., Jantz, P., Tape, K. D. & Goetz, S. J. Tundra plant aboveground biomass and shrub dominance mapped across the north slope of Alaska. *Environmental Research Letters* **13**, 035002 (2018).

[8] Myers-Smith, I. H. *et al.* Complexity revealed in the greening of the Arctic. *Nature Climate Change* **10**, 106–117 (2020).

[9] Frost, G. V. *et al.* Arctic report card 2021: Tundra Greenness. Tech. Rep. 21-08 (2021). URL https://doi.org/10.25923/8n78-wp73.

[10] Min, E. *et al.* The give and take of Arctic greening: differential responses of the carbon sink-to-source threshold to light and temperature in tussock tundra may be influenced by vegetation cover. *Communications Biology* **7**, 950 (2024).

[11] García Criado, M. *et al.* Plant diversity dynamics over space and time in a warming Arctic. *Nature* **642**, 653–661 (2025).

[12] Bjorkman, A. D. *et al.* Plant functional trait change across a warming tundra biome. *Nature* **562**, 57–62 (2018).

[13] Phoenix, G. K. & Bjerke, J. W. Arctic browning: extreme events and trends reversing arctic greening. *Global change biology* **22**, 2960–2962 (2016).

[14] Lara, M. J., Nitze, I., Grosse, G., Martin, P. & McGuire, A. D. Reduced arctic tundra productivity linked with landform and climate change interactions. *Scientific reports* **8**, 2345 (2018).

[15] Heijmans, M. M. *et al.* Tundra vegetation change and impacts on permafrost. *Nature Reviews Earth & Environment* **3**, 68–84 (2022).

[16] Phoenix, G. K. & Treharne, R. Arctic greening and browning: Challenges and a cascade of complexities (2022).

[17] Aalto, J. *et al.* A new era of bioclimatic extremes in the terrestrial Arctic. *Science Advances* **12**, eadw5698 (2026).

[18] Rocha, A. V., Blakely, B., Jiang, Y., Wright, K. & Curasi, S. Is arctic greening consistent with the ecology of tundra? Lessons from an ecologically informed mass balance model. *Environmental Research Letters* **13**, 125007 (2018).

[19] Maes, S. L. *et al.* Environmental drivers of increased ecosystem respiration in a warming tundra. *Nature* **629**, 105–113 (2024).

[20] Niu, S. *et al.* Temperature responses of ecosystem respiration. *Nature Reviews Earth & Environment* **5**, 559–571 (2024).

[21] Schwieger, S. *et al.* Tundraflux: A database of ecosystem respiration with biotic and abiotic metadata from Arctic and alpine tundra warming experiments. *Earth System Science Data Discussions* **2026**, 1–25 (2026).

[22] Luus, K. *et al.* Modeling the influence of snow cover on low Arctic net ecosystem exchange. *Environmental Research Letters* **8**, 035045 (2013).

[23] Shi, H. *et al.* Variability and uncertainty in flux-site scale net ecosystem exchange simulations based on machine learning and remote sensing: A systematic evaluation. *Biogeosciences Discussions* **2022**, 1–25 (2022).

[24] Natali, S. M. *et al.* Large loss of CO_2 in winter observed across the northern permafrost region. *Nature climate change* **9**, 852–857 (2019).

[25] Baldocchi, D. D. How eddy covariance flux measurements have contributed to our understanding of Global Change Biology. *Global change biology* **26**, 242–260 (2020).

[26] Parmentier, F.-J. W. *et al.* Longer growing seasons do not increase net carbon uptake in the northeastern Siberian tundra. *Journal of Geophysical Research: Biogeosciences* **116** (2011).

[27] Virkkala, A.-M. *et al.* Wildfires offset the increasing but spatially heterogeneous Arctic–boreal CO_2 uptake. *Nature Climate Change* **15**, 188–195 (2025).

[28] Natali, S. M. *et al.* NOAA Arctic Report Card 2024: Arctic Terrestrial Carbon Cycling. Tech. Rep. (2024). URL https://doi.org/10.25923/0gpp-mn10.

[29] Pallandt, M. M. *et al.* Representativeness assessment of the pan-Arctic eddy covariance site network and optimized future enhancements. *Biogeosciences* **19**, 559–583 (2022).

[30] Jung, M. *et al.* Global patterns of land-atmosphere fluxes of carbon dioxide, latent heat, and sensible heat derived from eddy covariance, satellite, and meteorological observations. *Journal of Geophysical Research: Biogeosciences* **116** (2011).

[31] Tramontana, G. *et al.* Predicting carbon dioxide and energy fluxes across global FLUXNET sites with regression algorithms. *Biogeosciences* **13**, 4291–4313 (2016).

[32] Jung, M. *et al.* Scaling carbon fluxes from eddy covariance sites to globe: synthesis and evaluation of the FLUXCOM approach. *Biogeosciences* **17**, 1343–1365 (2020).

[33] Nathaniel, J., Liu, J. & Gentine, P. MetaFlux: Meta-learning global carbon fluxes from sparse spatiotemporal observations. *Scientific Data* **10**, 440 (2023).

[34] Yuan, Q., Wang, X., Che, T. & Li, J. Global carbon flux dataset generated by fusing remote sensing and multiple flux networks observation. *Scientific Data* **12**, 1359 (2025).

[35] Zhu, S. *et al.* The UFLUX ensemble of multiple-scale carbon, water, and energy fluxes. *Scientific Data* (2025).

[36] Nelson, J. A. *et al.* X-BASE: the first terrestrial carbon and water flux products from an extended data-driven scaling framework, FLUXCOM-X. *Biogeosciences* **21**, 5079–5115 (2024).

[37] Porcar-Castell, A. *et al.* Linking chlorophyll a fluorescence to photosynthesis for remote sensing applications: mechanisms and challenges. *Journal of experimental*

botany **65**, 4065–4095 (2014).

[38] Guanter, L. *et al.* Global and time-resolved monitoring of crop photosynthesis with chlorophyll fluorescence. *Proceedings of the National Academy of Sciences* **111**, E1327–E1333 (2014).

[39] Magney, T. S. *et al.* Mechanistic evidence for tracking the seasonality of photosynthesis with solar-induced fluorescence. *Proceedings of the National Academy of Sciences* **116**, 11640–11645 (2019).

[40] Verma, M. *et al.* Effect of environmental conditions on the relationship between solar-induced fluorescence and gross primary productivity at an OzFlux grassland site. *Journal of Geophysical Research: Biogeosciences* **122**, 716–733 (2017).

[41] Chen, A. *et al.* Seasonal changes in GPP/SIF ratios and their climatic determinants across the Northern Hemisphere. *Global Change Biology* **27**, 5186–5197 (2021).

[42] Joiner, J. & Yoshida, Y. Global MODIS and FLUXNET-derived Daily Gross Primary Production, V2 (Version 2). ORNL Distributed Active Archive Center (2021). URL https://doi.org/10.3334/ORNLDAAC/1835. Date Accessed: 2026-03-18.

[43] Zhang, Y., Joiner, J., Alemohammad, S. H., Zhou, S. & Gentine, P. A global spatially contiguous solar-induced fluorescence (CSIF) dataset using neural networks. *Biogeosciences* **15**, 5779–5800 (2018). URL https://doi.org/10.5194/bg-15-5779-2018.

[44] Luijkx, I. *et al.* Global CO_2 gridded flux fields from 14 atmospheric inversions in GCB2025 (2025). URL https://meta.icos-cp.eu/objects/6gR_MW23fL2KEI860UX_TGoO.

[45] Ma, D. *et al.* Detection, mapping, and interpretation of the main drivers of the Arctic GPP change from 2001 to 2019. *Climate Dynamics* **62**, 723–738 (2024). URL https://doi.org/10.1007/s00382-023-06935-z.

[46] Yu, M., Cao, Y., Tian, J. & Ren, B. Increased Contribution of Extended Vegetation Growing Season to Boreal Terrestrial Ecosystem GPP Enhancement. *Remote Sensing* **17**, 83 (2024).

[47] Olefeldt, D. *et al.* The Boreal-Arctic Wetland and Lake dataset ($BAWLD$). *Earth System Science Data Discussions* **2021**, 1–40 (2021).

[48] Walker, D. A. *et al.* The Circumpolar Arctic vegetation map. *Journal of Vegetation Science* **16**, 267–282 (2005).

[49] See, C. R. *et al.* Decadal increases in carbon uptake offset by respiratory losses across northern permafrost ecosystems. *Nature Climate Change* 1–10 (2024).

[50] Hugelius, G. *et al.* Large stocks of peatland carbon and nitrogen are vulnerable to permafrost thaw. *Proceedings of the National Academy of Sciences* **117**, 20438–20446 (2020).

[51] Bouriaud, O. *et al.* A saturating response of photosynthesis to an increasing leaf area index allows selective harvest of trees without affecting forest productivity. *Biogeosciences* **22**, 4729–4741 (2025).

[52] Olefeldt, D. *et al.* Circumpolar distribution and carbon storage of thermokarst landscapes. *Nature communications* **7**, 13043 (2016).

[53] Miner, K. R. *et al.* Permafrost carbon emissions in a changing Arctic. *Nature Reviews Earth & Environment* **3**, 55–67 (2022).

[54] Ogden, E. L., Cumming, S. G., Smith, S. L., Turetsky, M. R. & Baltzer, J. L. Permafrost thaw induces short-term increase in vegetation productivity in northwestern Canada. *Global Change Biology* **29**, 5352–5366 (2023).

[55] Hua, H. *et al.* Accelerated land surface greening caused by earlier permafrost thawing. *Nature Communications* **17**, 920 (2025).

[56] Friedl, M., Sulla-Menashe, D. & MODAPS SIPS - NASA. MCD12C1 MODIS-/Terra+Aqua Land Cover Type Yearly L3 Global 0.05Deg CMG (2015). URL http://doi.org/10.5067/MODIS/MCD12C1.006.

[57] Raynolds, M. K. *et al.* A raster version of the Circumpolar Arctic Vegetation Map (CAVM). *Remote Sensing of Environment* **232**, 111297 (2019).

[58] Berner, L. T. *et al.* Summer warming explains widespread but not uniform greening in the Arctic tundra biome. *Nature Communications* **11**, 4621 (2020).

[59] Frost, G. V. *et al.* The changing face of the Arctic: four decades of greening and implications for tundra ecosystems. *Frontiers in Environmental Science* **13**, 1525574 (2025).

[60] Mekonnen, Z. A. *et al.* Arctic tundra shrubification: a review of mechanisms and impacts on ecosystem carbon balance. *Environmental Research Letters* **16**, 053001 (2021).

[61] Helbig, M. *et al.* Warming response of peatland CO_2 sink is sensitive to seasonality in warming trends. *Nature Climate Change* **12**, 743–749 (2022).

[62] Schuur, E. A., Crummer, K. G., Vogel, J. G. & Mack, M. C. Plant species composition and productivity following permafrost thaw and thermokarst in Alaskan tundra. *Ecosystems* **10**, 280–292 (2007).

[63] Schuur, E. A. & Mack, M. C. Ecological response to permafrost thaw and consequences for local and global ecosystem services. *Annual review of ecology, evolution, and systematics* **49**, 279–301 (2018).

[64] Maes, S. *et al.* Dataset for environmental drivers of increased ecosystem respiration in a warming tundra (2024).

[65] Niu, B. *et al.* Warming homogenizes apparent temperature sensitivity of ecosystem respiration. *Science Advances* **7**, eabc7358 (2021).

[66] López-Blanco, E. *et al.* Exchange of CO_2 in Arctic tundra: impacts of meteorological variations and biological disturbance. *Biogeosciences* **14**, 4467–4483 (2017).

[67] Zona, D. *et al.* Pan-arctic soil moisture control on tundra carbon sequestration and plant productivity. *Global Change Biology* **29**, 1267–1281 (2023). URL https://onlinelibrary.wiley.com/doi/abs/10.1111/gcb.16487.

[68] Zhang, W. *et al.* Process-oriented modeling of a High Arctic tundra ecosystem: Long-term carbon budget and ecosystem responses to interannual variations of climate. *Journal of Geophysical Research: Biogeosciences* **123**, 1178–1196 (2018).

[69] Zona, D. *et al.* Earlier snowmelt may lead to late season declines in plant productivity and carbon sequestration in Arctic tundra ecosystems. *Scientific Reports* **12**, 3986 (2022).

[70] Zona, D. *et al.* Pan-Arctic soil moisture control on tundra carbon sequestration and plant productivity. *Global Change Biology* **29**, 1267–1281 (2023).

[71] Kim, J. *et al.* Carbon response of tundra ecosystems to advancing greenup and snowmelt in Alaska. *Nature Communications* **12**, 6879 (2021).

[72] Drusch, M. *et al.* The FLuorescence EXplorer Mission Concept—ESA's Earth Explorer 8. *IEEE Transactions on Geoscience and Remote Sensing* **55**, 1273–1284 (2017).

[73] Su, W. *et al.* A new global carbon flux estimation methodology by assimilation of both in situ and satellite CO_2 observations. *npj Climate and Atmospheric Science* **7**, 287 (2024).

[74] Mavrovic, A. *et al.* Reviews and syntheses: Recent advances in microwave remote sensing in support of terrestrial carbon cycle science in Arctic–boreal regions. *Biogeosciences* **20**, 2941–2970 (2023).

[75] Widhalm, B. *et al.* InSAR-derived seasonal subsidence reflects spatial soil moisture patterns in Arctic lowland permafrost regions. *The Cryosphere* **19**, 1103–1133 (2025).

[76] Mikkonen, S. *et al.* Technical note: Effects of uncertainties and number of data points on line fitting – a case study on new particle formation. *Atmospheric Chemistry and Physics* **19**, 12531–12543 (2019).

[77] Rantanen, M. *et al.* Bioclimatic atlas of the terrestrial Arctic. *Scientific data* **10**, 40 (2023).

Methods

Data spatial and temporal harmonization

To harmonize all datasets onto a common grid over the terrestrial Arctic (i.e. latitudes $\geq 60°$N), all variables were re-gridded to a spatial resolution of $0.05° \times 0.05°$, covering latitudes 60°N–90°N and longitudes 180°W-180°E. The CSIF, FluxSat GPP, and X-BASE GPP and NEE datasets were spatially cropped to the study domain without

further interpolation, as their native resolution and grid already matched the target grid. Daily mean air temperatures from the ARCLIM dataset, originally derived from hourly ERA5-Land data at 0.1° resolution, were interpolated to the 0.05° grid. The growing season period of JJA is set to be consistent with the warming-induced experiment for the ER [19].

Among the ancillary land cover datasets, the IGBP land cover classification is originally provided on the target grid. The BAWLD land cover classes (glaciers and permanent snow, rocklands, dry tundra, boreal forest, wetlands, lakes, and rivers) were originally available as fractional coverage of each class at a resolution of $0.5° \times 0.5°$. Each class was rasterized individually from the shapefile to the common grid. After rasterizing onto the common grid, the dominant BAWLD land cover type for each grid cell was then defined as the class with the highest fractional coverage. All seven classes were represented, although the river class did not dominate in any grid cell. The CAVM land cover dataset, originally at 1 km × 1 km resolution, was resampled to the Arctic grid using mode resampling, assigning each target grid cell the most frequently occurring source class.

For temporal sampling, hourly X-BASE variables were aggregated to daily values by computing daily means, whereas all other datasets were already provided as daily values. Data was evaluated for the growing season, defined here as June–July– August (JJA).To ensure temporal consistency across datasets, all variables were subsampled to match the 4-day temporal resolution of the CSIF dataset, resulting in 23 observations per year. In 2020, however, the cSIF time series ended on the 9th of August, yielding only 18 observations for that year. The remaining datasets were subsampled to follow the same temporal sampling scheme as in previous years. FluxSat GPP values, originally provided in units of μmol CO_2 m^{-2} s^{-1}, were converted to gC m^{-2} day^{-1}.

The machine-learning-based carbon flux datasets included: FluxSat GPP, X-BASE GPP ($GPP_{X\text{-}BASE}$), and X-BASE NEE ($NEE_{X\text{-}BASE}$). In addition, three derived flux variables were defined as follows:

$\text{ER}_{\text{X-BASE}} = \text{NEE}_{\text{X-BASE}} + \text{GPP}_{\text{X-BASE}}$,

$\text{ER}_{\text{COM}} = \text{NEE}_{\text{X-BASE}} + \text{GPP}_{\text{FluxSat}}$,

$\text{NEE}_{\text{COM}} = \text{ER}_{\text{X-BASE}} - \text{GPP}_{\text{FluxSat}}$.

In total, six flux variables were analysed, comprising two GPP, two NEE, and two ER datasets.

Decadal and climatological means were computed for all temporally varying variables using the 4-day resolution JJA datasets. Decadal means were calculated separately for the periods 2001–2010 and 2011–2020, whereas the climatological mean was derived from the full 2001–2020 time series.

Reported main statistics

All summary statistics in the main text and TableA3 are reported as medians rather than means, as no explicit filtering of outliers was applied to the flux distributions. Given their potentially skewed and non-Gaussian nature, the median provides a more robust and representative measure of central tendency, minimizing the influence of extreme values. Interquartile ranges (IQRs) are also reported, corresponding to the 25th and 75th percentiles.

Statistics provided in Tables A3 and A2 include the metrics of mean, median, minimum, maximum, standard deviation, number of pixels evaluated, and the 25th and 75th percentiles.

C flux and SIF air temperature sensitivity

To quantify the sensitivity of SIF and carbon flux variables (GPP, ER, NEE) to air temperature, a linear relationship of the form $f(x) = \alpha x + n$ was assumed, where $f(x)$ denotes the anomaly of the response variable (δSIF, δGPP, δER, δNEE) and $x = \delta T_{air}$ represents the air temperature anomaly. Anomalies were defined relative to the climatological mean over the period 2001–2020. For example, for temperature, $\delta T_a = T_a - T_{mean}$, where T_a corresponds to the 4-day observations and T_{mean} corresponds to the climatological mean. An analogous definition was applied to all response variables.

The regression analysis was conducted using Orthogonal Distance Regression (ODR), which accounts for uncertainties in both dependent and independent variables. The implementation was carried out using the SciPy ODR package. This method was selected due to its robustness in the presence of higher uncertainties and outliers, particularly when uncertainties are estimated from the data [76].

Uncertainties were assigned at the 4-day temporal resolution for all variables. The conversion from absolute values to anomalies was assumed to represent a constant shift and, therefore, not to introduce additional uncertainty. Consequently, uncertainties of the anomaly variables were assumed to be equal to those of the original values. For air temperature, a constant uncertainty of 0.21°C was applied, based on the reported summer mean bias between station observations and ERA5-Land data [77]. For clear-sky daily SIF, the uncertainty was defined as 11% of the daily value, with a minimum threshold of 0.08 mW m^{-2} nm^{-1} sr^{-1}, reflecting an approximately 11% overestimation relative to the daily average satellite-based SIF, with RMSE below the minimum threshold [43]. For X-BASE GPP and NEE, which were derived from hourly data, uncertainty was estimated using the standard error of the daily mean, computed as $\sigma = \sigma_{\text{daily}}/\sqrt{24}$. For FluxSat GPP, the uncertainty provided with the dataset was used. For the derived flux variables (ERX-BASE, ERcombined, and $\text{NEE}_{\text{combined}}$), uncertainties were propagated assuming independent errors using standard error propagation, i.e. $\sigma = \sqrt{\sigma_1^2 + \sigma_2^2}$.

The statistical significance of the regression slopes was assessed using a two-sided Student's t-test. Resulting p-values were classified into two categories ($p<0.05$ and $p\geq0.05$) and visualized in Fig.A9. Model performance was further evaluated using the coefficient of determination (R^2). Only regions exhibiting statistically significant relationships ($p<0.05$) and sufficiently high explanatory power ($R^2>0.15$) are presented in Fig. A10. Spatial distributions of R^2 are shown in the right upper panels of Fig.A9.

NEE Probability Density Function (PDF) and Net PDF

Probability density functions (PDFs) were computed for each CAVM class using all available NEE values over the 2001–2020 period during the growing season (JJA) (Fig. A11). These PDFs were normalized such that the total area under each distribution equals one.

We then defined the net PDF as the difference between the integrated areas corresponding to positive and negative NEE values. Positive NEE values represent carbon release to the atmosphere, whereas negative values indicate carbon uptake. Accordingly, a negative (positive) net PDF reflects a dominance of carbon uptake (carbon release) for a given CAVM class and year.

1 Data availability

Carbon flux and Solar-induced Chlorophyll Fluorescence (SIF) dataset

Data are available from the following sites. The Solar-induced Chlorophyll Fluorescence (SIF) cSIF product [43] was downloaded from . We use the cSIF *clear* dataset. The X-BASE data [36] was accessed through the repository available in https://gitlab.gwdg.de/fluxcom/fluxcomxdata. Hourly values were downloaded to compute daily averages at a 0.05-degree resolution (see Methods). FluxSat [42] dataset was downloaded from NASA's Earthdata repository https://search.earthdata.nasa.gov/. Ecosystem Respiration (ER) percent maps of increase due to warming were downloaded from the Zenodo repository https://doi.org/10.5281/zenodo.10572479 associated with [64].

Classification maps

The BALWD classification maps [47] were downloaded from https://doi.org/10.18739/A2C824F9X.. The CAVM [57] Arctic vegetation map can be accessed from https://data.mendeley.com/datasets/c4xj5rv6kv/2.

The IGBPS land-cover classification map [56] was downloaded from https://www.earthdata.nasa.gov/data/catalog/lpcloud-mcd12c1-006 (we used data from 2020). The Thermokarst presence classification map (used in Supplementary Material Tables) [52] was downloaded from https://dx.doi.org/10.3334/ORNLDAAC/1332.

Atmospheric inversion net C flux model

Data was accessed from https://meta.icos-cp.eu/objects/6gR_MW23fL2KEI860UX_TGoO under the Creative Commons Attribution 4.0 international licence . https://creativecommons.org/licenses/by/4.0/legalcode. The downloaded package was `GCP2025_inversions_1x1_version1_0_20251031.nc` [44] with PID 10.18160/VZ3B-GHYQ. We used the field land_flux_only_fossil_cement_adjusted

2 Code availability

All Python code used in this study is made available through the GitHub repository (https://github.com/TUT-ISI/TundraBoreal_SIF_GPP_NEE_ER.git).

3 Acknowledgements

N.S. and E.K. acknowledge funding from the Research Council of Finland (RcF) (grant no. 366937). T.T. acknowledges funding from the RcF (grant no. 330165) and ACCC Flagship (grant no. 337552). A.V. acknowledges funding from the RcF (grant no. 371479.). S.VW. acknowledges ERC-2021-STG project (grant no. 101041768).

4 Authors contributions

N.S. designed the study, coded the plots and analysis, and wrote the paper. E.K. coded the plots, contributed to discussions and analysis, and participated in writing the paper. A.V. and T.T. provided feedback on the data analysis and the process, as well as contributed to the manuscript during reviews. A.L., J.A., M.L., S.VW., and

P.K. reviewed and contributed to the writing and discussion. A.A. contributed to the design of the study, discussion and reviewed and commented on the manuscript.

5 Funding

This study was funded by the Research Council of Finland project ArcticSIF (grant no. 366937).

6 Competing interests

The authors declare that they have no competing interests.

7 Additional information

Supplementary information The online version contains supplementary Materials are available at xx.

Correspondence and requests for materials should be addressed to Neus Sabater.

Supplementary Files

This is a list of supplementary files associated with this preprint. Click to download.

- SabateretalSupplementary.pdf